Article

TiO2 Inverse Opals Modified by Ag Nanoparticles: A Synergic Effect of Enhanced Visible-Light Absorption and Efficient Charge Separation for Visible-Light Photocatalysis

Thanh-Hiep Thi Le [1], Thanh-Trang Bui [2], Hao Van Bui [3,4,*], Van-Duong Dao [5] and Loan Le Thi Ngoc [2,*]

1 Office of Scientific Research and Technology, Duy Tan University, Da Nang 550000, Vietnam; letthanhhiep@dtu.edu.vn
2 Faculty of Natural Sciences, Quy Nhon University, Quy Nhon 55113, Vietnam; buithanhtrang@qnu.edu.vn
3 Faculty of Materials Science and Engineering, Phenikaa University, Yen Nghia, Ha-Dong District, Hanoi 12116, Vietnam
4 Faculty of Electrical and Electronic Engineering, Phenikaa University, Yen Nghia, Ha-Dong District, Hanoi 12116, Vietnam
5 Faculty of Biotechnology, Chemistry and Environmental Engineering, Phenikaa University, Yen Nghia, Ha-Dong District, Hanoi 12116, Vietnam; duong.daovan@phenikaa-uni.edu.vn
* Correspondence: hao.buivan@phenikaa-uni.edu.vn (H.V.B.); lethingocloan@qnu.edu.vn (L.L.T.N.); Tel.: +84-868-015-368 (H.V.B.); +84-961-960-639 (L.L.T.N.)

Abstract: This work reports on the synthesis, characterization, and photocatalytic performance of the TiO2 inverse opal nanostructure (IP-TiO2) and the IP-TiO2 modified by Ag nanoparticles (Ag@IP-TiO2). The IP-TiO2 is fabricated using polystyrene spheres as the template and TiCl4 as the precursor, and the Ag@IP-TiO2 is realized by photoreduction method. The morphological, structural, and optical properties of the materials are investigated by scanning electron microscopy, X-ray diffraction, ultraviolet–visible (UV-VIS) absorption spectroscopy, and photoluminescence spectroscopy. Their photocatalytic performances are studied by the degradation of rifampicin antibiotic under the visible-light irradiation generated by an LED lamp. The results demonstrate that the IP-TiO2 is composed of mesopores arranged in the honeycomb structure and strongly absorbs visible light in the wavelength range of 400–500 nm. This facilitates the visible-light catalytic activity of IP-TiO2, which is further enhanced by the surface modification by Ag nanoparticles. Our studies on the UV-VIS absorption and photoluminescent properties of the materials reveal that the presence of Ag nanoparticles not only enhances the visible-light absorption of IP-TiO2, but also reduces the recombination of photogenerated electrons and holes. These two factors create a synergic effect that causes the enhanced photocatalytic performance of Ag@IP-TiO2.

Keywords: titanium dioxide; inverse opals; visible-light photocatalysis; rifampicin degradation; charge separation

1. Introduction

Water pollution caused by antibiotics has been a severe environmental issue in recent years, especially in developing countries [1,2]. To address this issue, various methods have been developed, including molecular absorption, biodegradation, photodegradation, and oxidation [1,3]. Photocatalysis is an important technique that is popularly used in environmental applications due to its commerciality, nontoxicity, and renewable capacity [4]. This technique uses photocatalysts in combination with light to facilitate the chemical reactions on the catalyst surface [5]. Much effort has been made to utilize sunlight as the energy source in photocatalysis because of its omnipresence and abundance on earth. Therefore, achieving materials that are photocatalytically active and efficient under sunlight irradiation is an important target in photocatalysis for real life applications [4].

Titanium dioxide (TiO$_2$) is a widely used photocatalyst in many environmental and energy-related applications due to its excellent photoactivity, high chemical stability, and low cost [6]. However, a major disadvantage of TiO$_2$ is that it does not absorb visible light due to its large bandgap (i.e., ~3.2 eV) [6,7]. As a consequence, TiO$_2$ does not harvest and utilize sunlight efficiently, which limits its practical applications. Considerable attempts have been made to enable the optical absorption and facilitate the photocatalytic activity of TiO$_2$ under visible light irradiation [8]. Doping, which is done by introducing other elements (i.e., dopants) into the TiO$_2$ lattice, is the most popular way to achieve this goal [9]. In doped TiO$_2$, the dopant atoms create defects in the TiO$_2$ crystalline structure, thereby generating energy levels in the band gap of TiO$_2$ (i.e., the mid-gap levels). This effectively reduces the bandgap of TiO$_2$, resulting in the red shift of the optical absorption [5,10–12]. Black TiO$_2$, which is generally undoped TiO$_2$ but contains defect species like Ti^{3+} and oxygen vacancies, is a high-efficiency visible-light photocatalyst that has attracted enormous attention in the last decade [13–15]. It is believed that these defects are responsible for the enhanced photoactivity of black TiO$_2$. Nevertheless, it is not always that the photocatalytic performance of black TiO$_2$ is higher than that of pristine TiO$_2$. In fact, there are other factors that govern the catalytic properties of black TiO$_2$ such as defect concentration, defect location, synthesis methods, and conditions, etc., which requires better understanding to achieve the photocatalysts with desired properties [16].

In the recent years, photocatalysts based on inverse opal TiO$_2$ (IP-TiO$_2$) nanostructures have attracted great attention due to their excellent visible-light photocatalytic activities [17–26]. Without the need of doping, IP-TiO$_2$ can absorb visible-light due to slow photon effect caused by the multiple light scattering in the periodic inverse opal structure [26,27]. In addition, similarly to other types of TiO$_2$ nanomaterials, the coupling of IP-TiO$_2$ and metal nanoparticles (NPs) such as Au [26], Ag [28], or Ni [29], can boast several advantages in photocatalysis. On the one hand, this coupling may enhance the visible-light absorption due to the localized surface plasmon resonance (LSPR) effect of the NPs, thereby improving the light harvesting efficiency of the catalysts. On the other hand, the lower Fermi level of noble metals with respect to the conduction band of TiO$_2$ facilitates the transfer of photogenerated electrons from TiO$_2$ to the metal. This increases the charge separation, which consequently improves the photocatalytic efficiency [26,30]. Therefore, IP-TiO$_2$ has emerged as a novel class of nanostructured photocatalysts that is promising for environmental and energy-related applications [17–26].

Although numerous studies on the synthesis, characterization, and photocatalytic properties of IP-TiO$_2$ have been reported [18,28,31,32], research on the photocatalytic performance of IP-TiO$_2$ in antibiotic photodegradation is still limited. Here, we report on the synthesis of IP-TiO$_2$ and IP-TiO$_2$ modified by Ag NPs (Ag@IP-TiO$_2$) and study their performance in the degradation of rifampicin (RIF) antibiotic under visible-light irradiation for the first time. We demonstrate that IP-TiO$_2$ strongly absorbs visible light and exhibits excellent photocatalytic activity, which is considerably higher than the commercial P25 TiO$_2$ photocatalyst. The surface modification of IP-TiO$_2$ by Ag NPs results in a significant enhancement of the photocatalytic performance. By combining X-ray diffraction, UV-VIS absorption and photoluminescent spectroscopies, the structural and optical properties of the materials are investigated. The results reveal that the presence of Ag NPs not only increases the visible-light absorption, but also reduces the charge recombination, both of which together lead to the enhanced photocatalytic performance of IP-TiO$_2$. Therefore, our work not only provides a deeper understanding of the visible-light photocatalytic activity of IP-TiO$_2$ and Ag@IP-TiO$_2$, but also demonstrates their potential application in tackling the environmental issues caused by antibiotics.

2. Results and Discussion

2.1. Morphology and Crystalline Structure of IP-TiO$_2$ and Ag@IP-TiO$_2$

The scanning electron microscopy (SEM) images of the synthesized polystyrene (PS) spheres are shown in Figure 1a,b. The image in Figure 1a demonstrates an assembly of PS spheres that forms a well-ordered 3D structure. The image acquired with a higher

magnification (Figure 1b) reveals a smooth surface of the PS spheres. Using Gatan DigitalMicrograph$^{\circledR}$ software (Version 2.31.734.0, © 1996–2014 Gatan Inc., Pleasanton, CA, USA), the diameters of the spheres (d_1) are measured; an average diameter of 340 nm is obtained, which is accompanied by a standard deviation of 4 nm. This value indicates a very narrow particle size distribution of the PS spheres. The SEM images of the IP-TiO$_2$ are shown in Figure 1c,d. The structure contains hexagonal inverse opals arranged in the honeycomb geometry. The average diameter of the inverse opals (d_2) is 249 nm with a standard deviation of 9 nm, whereas the average thickness of the wall between two adjacent inverse opals (t_2) is in the range of 15–25 nm. The three large holes in each inverse opal originate from its contacting areas with three adjacent PS spheres before they are removed during the annealing. The inverse opals and the holes provide a high surface area and effective open space for adsorption and transport of molecules in catalytic processes [33].
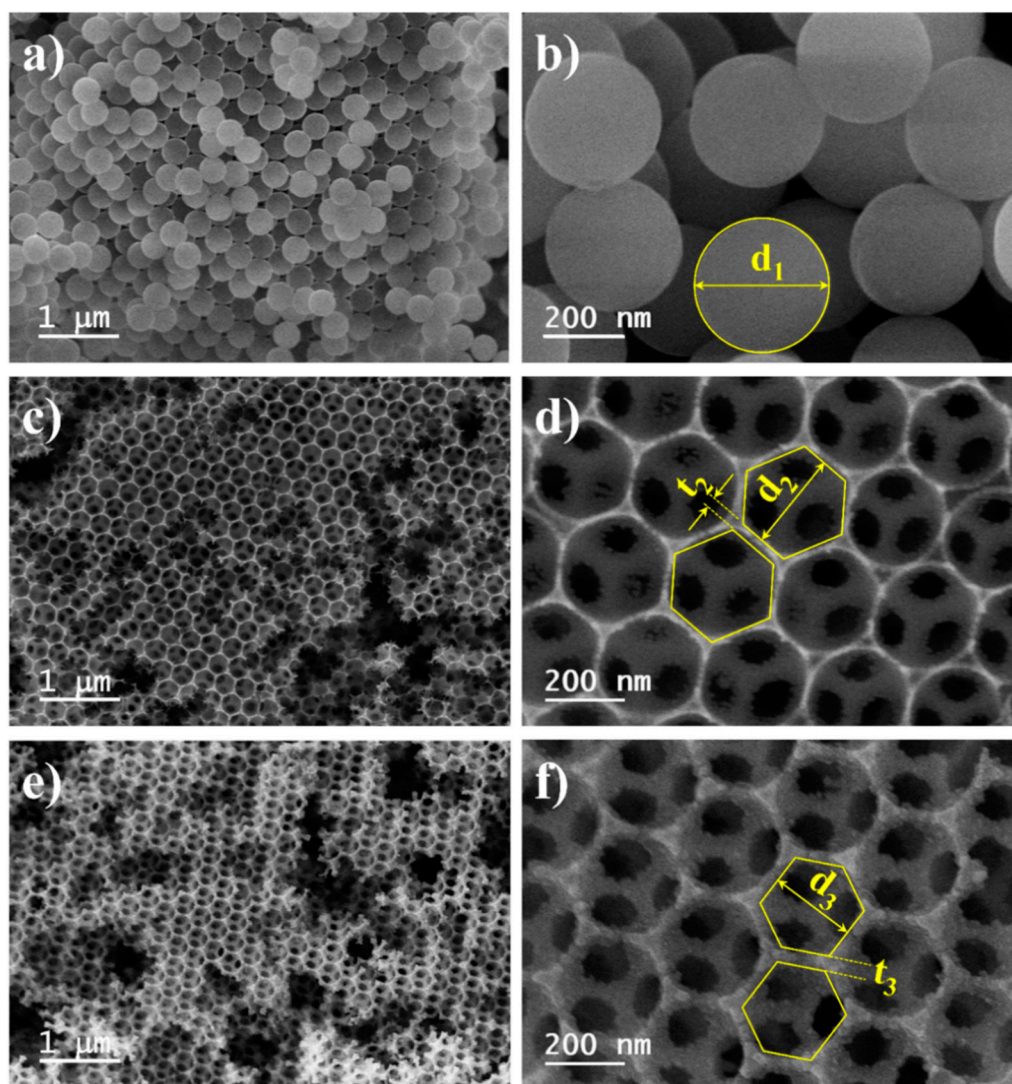
Figure 1. SEM images of (**a**,**b**) the PS spheres, (**c**,**d**) IP-TiO$_2$, and (**e**,**f**) Ag@IP-TiO$_2$; the images on the right side (**b**,**d**,**f**) are acquired with a higher magnification.

The morphology of the IP-TiO$_2$ after the deposition of Ag NPs is demonstrated in Figure 1e,f. The SEM images indicate that the arrangement of the inverse opals is preserved. However, due to the presence of Ag NPs, the surface of the inverse opals becomes rougher. The deposition of Ag NPs also results in a decrease in diameter of the inverse opals (d_3) and an increase in thickness of the wall between two adjacent inverse opals (t_3). In particular, the average diameter is 243 nm and the wall thickness varies between 25 and 35 nm.

The X-ray diffraction (XRD) patterns of the synthesized IP-TiO$_2$ and Ag@IP-TiO$_2$ are shown in Figure 2. The peaks at 25.2°, 38.3°, 48.2°, 54.3°, 55.4°, and 62.9° in the pattern of IP-TiO$_2$ represent the diffraction on the (101), (112), (200), (105), (211), and (204) planes of the anatase phase of TiO$_2$ (JCPDS 21-12768). No diffraction peak of the rutile phase is observed, suggesting the single phase of the IP-TiO$_2$ crystalline structure. The XRD pattern of Ag@IP-TiO$_2$ shows two additional peaks at 44.3° and 64.7°. These peaks represent the (200) and (220) planes of the face-centered cubic (FCC) structure of Ag (JCPDS 21-12768). Together with the SEM images shown in Figure 1, the XRD patterns confirm the successful synthesis of IP-TiO$_2$ and the subsequent deposition of Ag NPs to achieve Ag@IP-TiO$_2$.
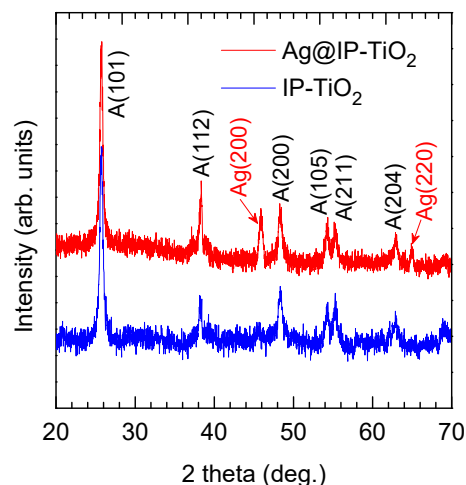
Figure 2. XRD patterns of the IP-TiO$_2$ (**bottom**) and Ag@IP-TiO$_2$ nanomaterials (**top**).

2.2. Optical Properties of IP-TiO$_2$ and Ag@IP-TiO$_2$

The UV-VIS absorption spectra of the synthesized IP-TiO$_2$ and Ag@IP-TiO$_2$ are shown in Figure 3. For comparison, the spectrum of the commercial P25 TiO$_2$ nanopowder is also included. All the spectra exhibit strong absorption in the UV spectral region with a steep edge at about 380 nm. This edge represents the band-to-band absorption of bulk TiO$_2$ materials [34]. Importantly, whereas P25 TiO$_2$ shows no absorption in the visible spectral region, IP-TiO$_2$ and Ag@IP-TiO$_2$ exhibit strong visible-light absorption with two distinct regions: a relatively broad absorption range between 400 and 500 nm, and an extended absorption from 500 nm toward the longer wavelengths. These absorption ranges have been reported as the first-order and higher-order absorption that arises from the slow photon effect due to the multiple light scattering in the periodic inverse opal structure [18,28,31,32,35]. However, while studying the photoluminescent properties of the IP-TiO$_2$, we observe a strong emission band with a peak at 420 nm (Figure 4). As discussed in the following part, this strong luminescence indicates the presence of defects such as oxygen vacancies (V$_O$) on the TiO$_2$ surface [36–38]. These defects create the energy levels in the bandgap of TiO$_2$, enabling the sub-band transitions that cause the absorption of photons in the visible region. Hence, we attribute the absorption of IP-TiO$_2$ in the range between 400 and 500 nm to the presence of defects of TiO$_2$. This absorption can be enhanced by the multiple light scattering in the inverse opal structure that improves the light harvesting [28,31]. For the Ag@IP-TiO$_2$, the light absorption in this region is significantly enhanced. This enhancement is attributed to the plasmonic excitation of the Ag NPs in coupling of the multiple scattering effect of the inverse opal structure, which has been reported in the literature [28,31]. The UV-VIS spectra demonstrate that both IP-TiO$_2$ and Ag@IP-TiO$_2$ strongly absorb visible light. This is a key factor that facilitates the photocatalytic response of the photocatalysts under visible-light irradiation as discussed in the following part.
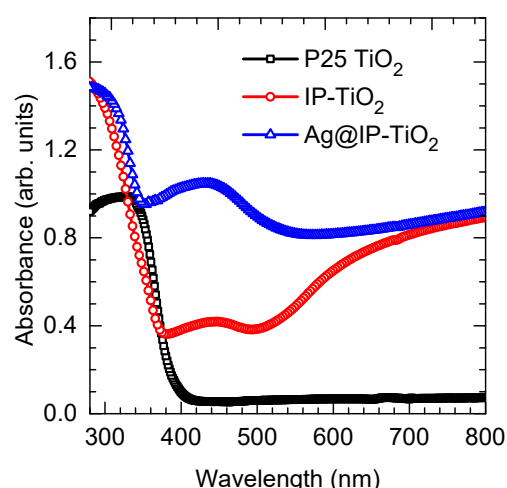
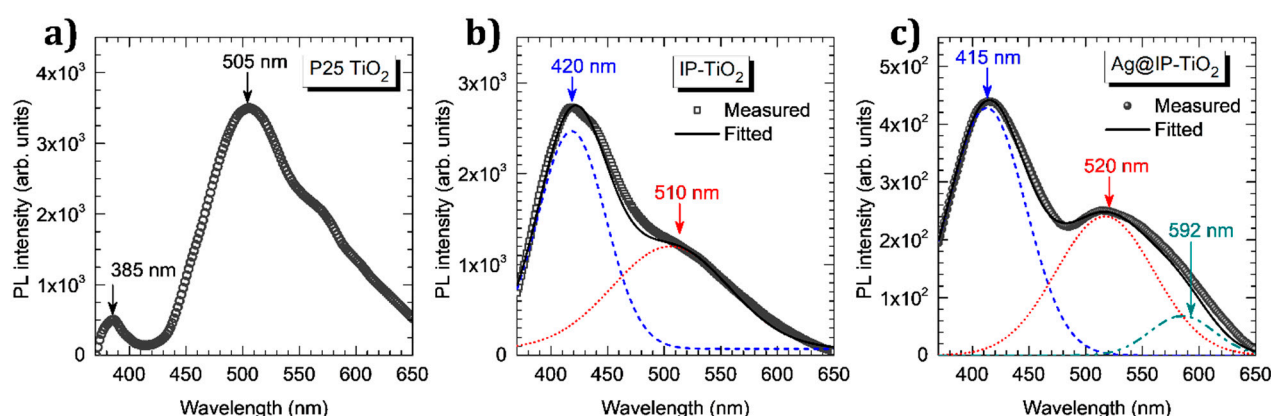**Figure 3.** UV-VIS absorption spectra of P25 TiO$_2$, IP-TiO$_2$, and Ag@IP-TiO$_2$.

Figure 4. PL spectra of (**a**) P25 TiO$_2$, (**b**) IP-TiO$_2$, and (**c**) Ag@IP-TiO$_2$.

The photoluminescence (PL) spectra of P25 TiO$_2$, IP-TiO$_2$, and Ag@IP-TiO$_2$ are shown in Figure 4. The spectrum of P25 TiO$_2$ (Figure 4a) exhibits two emission peaks at 385 nm and 505 nm. The emission with the peak at 505 nm arises from the radiative recombination of conduction electrons with trapped holes in TiO$_2$ [38–40]. This peak is also observed in the PL spectra of IP-TiO$_2$ (Figure 4b) and Ag@IP-TiO$_2$ (Figure 4c) with a small shift toward the longer wavelengths (i.e., 510 nm for IP-TiO$_2$ and 520 nm for Ag@IP-TiO$_2$). In the PL spectrum of P25 TiO$_2$, the emission with the peak at 385 nm is attributed to the band-to-band transitions (i.e., direct recombination). It is known that P25 TiO$_2$ contains both anatase and rutile phases, in which the anatase phase possesses an indirect bandgap, and the rutile phase possesses a direct bandgap [41]. As the direct recombination in an indirect bandgap semiconductor is prohibited, the emission peak at 385 nm is from the rutile TiO$_2$ [41].

The PL spectrum of IP-TiO$_2$ (Figure 4b) is deconvoluted into two components with two peaks at 420 and 510 nm. The first component with the peak at 420 nm is the excitonic PL. This PL arises from the two-stage transitions of excited electrons: non-radiative transitions from the conduction band to the sub-band energy levels in the bandgap, and the subsequent radiative transitions from the sub-band energy levels to the valence band [36]. The sub-band energy levels that enable excitonic PL is commonly caused by surface oxygen vacancies (VO) and surface defects [36–38]. Therefore, the high intensity of the excitonic PL peak (i.e., with respect to the intensity of the peak at 510 nm) suggests that the IP-TiO$_2$ contains high surface defect density. This is consistent with the light absorption in the visible region as discussed above. It is worth noting that in the PL spectrum of IP-TiO$_2$, the emission due to

band-to-band transition with the peak at 385 nm is not observed. This is due to the absence of the rutile phase in the synthesized TiO_2 inverse opal structure, which is indicated by the XRD patterns in Figure 2.

The comparison of the two PL spectra in Figure 4b,c shows that the PL intensity of Ag@IP-TiO_2 is nearly an order of magnitude lower than that of IP-TiO_2. The decrease in PL intensity indicates that the recombination of excited electrons and holes is reduced, which can be explained by the charge transfer between TiO_2 and Ag NPs. Namely, as the Fermi level of Ag is below the conduction band of TiO_2, excited electrons are facilitated to transfer from TiO_2 to Ag before they recombine with holes in the valence band [42]. This enhances the charge separation, which consequently increases photocatalytic activity of IP-TiO_2 as demonstrated below. We note that the deconvolution of the PL spectrum of Ag@IP-TiO_2 shows an additional component with a peak at 592 nm (Figure 4c). This emission can be due to the recombination of electrons localized in trap states with holes in the valence band [36].

2.3. Photocatalytic Activity of IP-TiO_2 and Ag@IP-TiO_2

The photocatalytic activity of IP-TiO_2 and Ag@IP-TiO_2 was tested by the degradation of RIF solution under visible-light irradiation generated by a LED lamp. For comparison, the performance of the commercial catalyst P25 TiO_2 under identical experimental conditions was also added. Prior to the irradiation, the suspension containing the solid catalyst and the RIF solution was continuously stirred in the dark for 90 min to achieve an adsorption–desorption equilibrium. We observed that at the equilibrium, the concentration of RIF decreased 14%, 10%, and 15% for P25 TiO_2, IP-TiO_2, and Ag@IP-TiO_2, respectively (Figure 5a). This small difference suggests that the specific surface areas of the IP-TiO_2 and Ag@IP-TiO_2 are comparable to that of P25 TiO_2, which is approximately 54 m^2 g^{-1} [39].

The change of the UV-VIS spectra of the RIF solution caused by the three catalysts under the visible-light irradiation is shown in Figure 5b–d. The spectra were acquired after every 30 min of irradiation. From these spectra, the decrease in intensity of the peak at the wavelength of 472 nm was used to determine the decrease in concentration of the RIF solution as a function of irradiation time, which is shown in Figure 5e. For comparison, the photolysis of RIF (i.e., the self-degradation without any catalyst) is also included. The results indicate that the photolysis of RIF is insignificant, whereas P25 TiO_2 only causes a small degradation, i.e., up to 25% after 180 min of irradiation. The latter is due to the fact that P25 TiO_2 does not absorb visible light, which is evidenced by the UV-VIS absorption spectrum shown in Figure 3. At the same time, 50% of RIF is degraded by IP-TiO_2, which further increases to 70% for Ag@IP-TiO_2. From the linear regression of kinetic plots shown in Figure 5f, the first-order degradation rates are determined [43]. For P25 TiO_2, a rate of 1.52×10^{-3} min^{-1} is achieved, which is above three times higher than the self-degradation rate (i.e., 0.42×10^{-3} min^{-1}). For IP-TiO_2 and Ag@IP-TiO_2, the rates are 3.64×10^{-3} and 5.92×10^{-3} min^{-1}, respectively. These numbers indicate the considerably higher photocatalytic activity of the catalysts based on the inverse opal structure with respect to the commercial P25 TiO_2.

The higher photocatalytic activity of IP-TiO_2 in comparison with P25 TiO_2 is explained by its capability of visible-light absorption, as indicated by the UV-VIS absorption spectra shown in Figure 3. This absorption facilitates the generation of electron-hole pairs, which subsequently causes the degradation of RIF. It has been demonstrated that the degradation of RIF is mainly caused by holes, whereas the contribution of other active species such as hydroxyl radicals (OH*) and superoxide ions (O^{2-}) is negligible [44]. The improved photocatalytic performance of Ag@IP-TiO_2 can be attributed to the key role of Ag NPs in the suppression of charge recombination. As demonstrated in Figure 4, the lower intensity of the PL emission band with the peak at 415–420 nm observed for Ag@IP-TiO_2 (Figure 4c) with respect to IP-TiO_2 (Figure 4b) indicates that the electron-hole recombination in Ag@IP-TiO_2 is reduced [45]. This can be explained that Ag NPs can act as electron sinks that facilitate the transfer of photogenerated electrons from TiO_2 to Ag NPs [42,46]. As

a consequence, the lifetime of holes is increased, thereby improving the photocatalytic performance of IP-TiO$_2$. In addition, the strong absorption in the visible region of Ag@IP-TiO$_2$ shown in Figure 3 indicates the strong plasmon resonance on the surface of Ag NPs. This can create a strong electric near-field in the vicinity of the Ag NPs, which can boost the generation of electron-hole pairs in TiO$_2$, and therefore enhance the photocatalytic performance [47]. This phenomenon is known as plasmonic photocatalysis, which was first observed for the Ag/TiO$_2$ system by Awazu et al. [47].
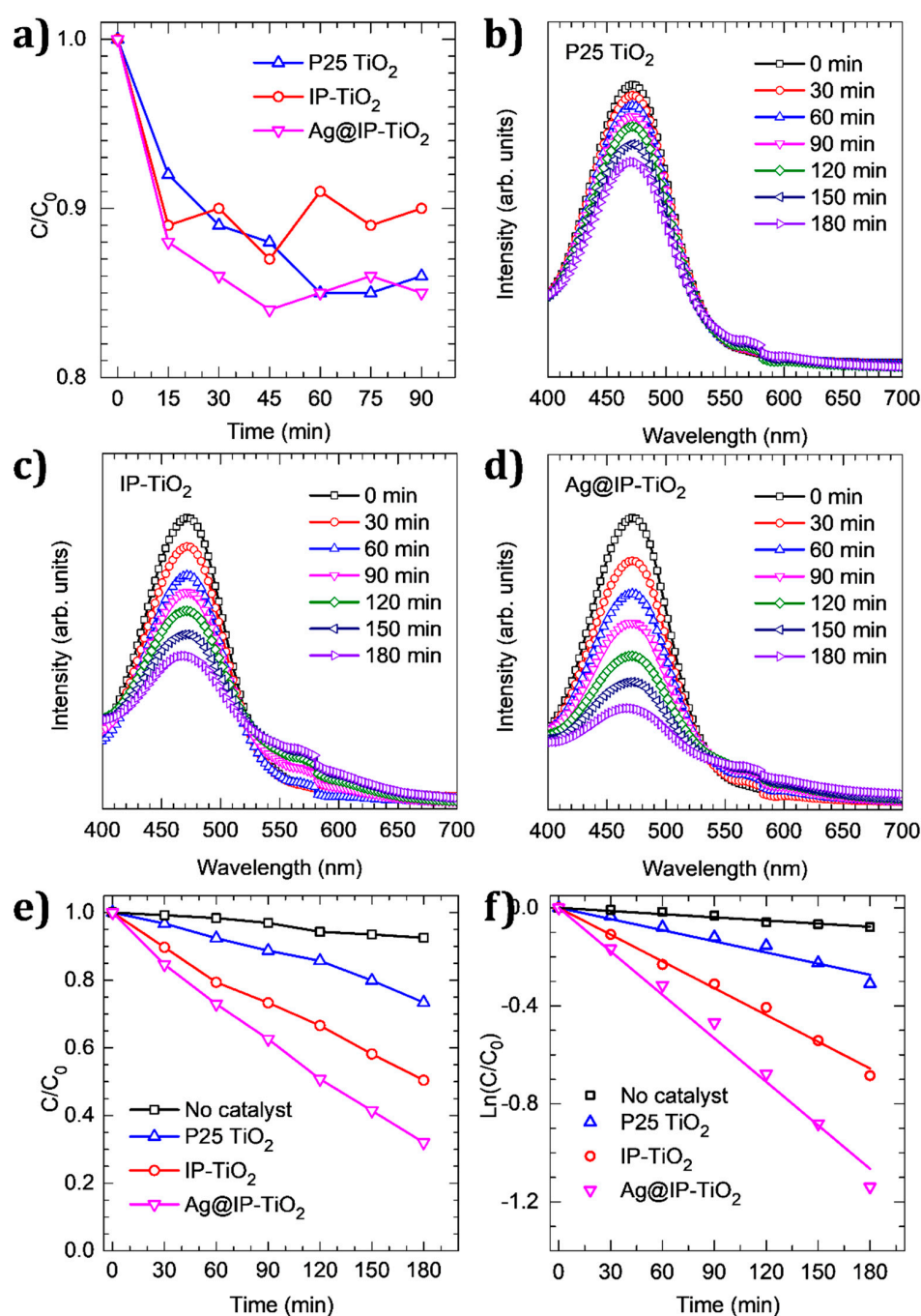
Figure 5. (**a**) adsorption of RIF on the catalyst surface before illumination; UV-VIS spectra of RIF solution as a function of irradiation time in the photocatalytic degradation caused by (**b**) P25 TiO$_2$, (**c**) IP-TiO$_2$, and (**d**) Ag@IP-TiO$_2$; (**e**) degradation curves of RIF as a function of exposure time and (**f**) the corresponding kinetic plots.

3. Materials and Methods

3.1. Materials

Sodium dodecyl sulfate (SDS), potassium persulfate (PPS), polyvinylpyrrolidone (PVP, MW = 360,000 g mol^{-1}), styrene monomers, aluminum oxide microparticles (Al_2O_3), titanium chloride ($TiCl_4$), ethanol, silver nitrate ($AgNO_3$), and rifampicin (RIF) were purchased from Sigma-Aldrich Co., Ltd., St. Louis, MO, USA.

3.2. Methods

3.2.1. Synthesis of Polystyrene Spheres

The synthesis of polystyrene (PS) spheres follows the experimental procedure developed by Cho et al. [48], in which SDS was used as the surfactant and PPS as the initiator. In a typical process, 8 mg of SDS and 100 mg of PPS were dissolved in 30 mL of deionized water at 70 °C and continuously stirred for 2 h under a continuous supply of N_2 gas. Hereafter, 6 mL of styrene monomers, which were filtered by Al_2O_3 to remove the polymerization inhibitors [49], was rapidly injected to the solution. The polymerization at 70 °C for 4 h resulted in PS spheres with an average diameter of 340 nm.

3.2.2. Synthesis of IP-TiO_2

IP-TiO_2 was grown on glass substrates, which were placed vertically in a 100 mL glass beaker containing 50 mL of solution of the as-synthesized PS spheres (1 mL), deionized water (35 mL), and ethanol (14 mL). The temperature of the beaker was maintained at 60 °C until the evaporation was complete. After that, $TiCl_4$ solution (0.2 M) was slowly dropped on the as-prepared glass substrates, which were then dried in air at 90 °C for 1 h, followed by a calcination at 450 °C in synthetic air for 2 h. During this stage, $TiCl_4$ was oxidized and converted into TiO_2, and the PS template was removed.

3.2.3. Synthesis of Ag@IP-TiO_2

Ag NPs nanoparticles were deposited on IP-TiO_2 by photoreduction method [50]. Firstly, 0.01 g of PVP was dissolved in 40 mL of ethylene glycol and continuously stirred for 30 min at room temperature to obtain a homogeneous solution. Then, 3 mL of $AgNO_3$ solution (1 M) was slowly added to the solution, which was further continuously stirred for 15 min to obtain a homogeneous suspension. In the next step, the as-prepared IP-TiO_2 on glass substrates were immersed into this suspension and irradiated by UV light for 20 min. The substrates were then washed in distilled water and finally dried in air at 60 °C for 12 h. The experimental procedures for the synthesis of PS, IP-TiO_2, and Ag@IP-TiO_2 are summarized by the schematic diagram shown in Figure 6.

3.2.4. Material Characterizations

The morphology of the synthesized materials was investigated by scanning electron microscopy (SEM) using a Hitachi S4800 FE-SEM (Ibaraki, Japan). Their crystalline structure was investigated by X-ray diffraction (XRD) technique using a Bruker D8 Advance Eco diffractometer (Bruker, Billerica, MA, USA). UV-VIS absorption spectra of the materials were measured by a JASCO V-750 UV-VIS Spectrophotometer (Easton, MD, USA). The photoluminescence (PL) spectra of the materials were recorded by using a Horiba Fluorolog®-3 spectrofluorometer (Agilent, Santa Clara, CA, USA) equipped with a laser of 350 nm excitation wavelength.

3.2.5. Photocatalytic Study

The photocatalytic performance of IP-TiO_2 and Ag@IP-TiO_2 was tested by the degradation of RIF antibiotic under visible light generated by a white-LED lamp (30 W) that had the emission spectrum only in the visible region (Figure 7). For the catalytic tests, IP-TiO_2 and Ag@IP-TiO_2 were peeled off from the glass substrates and ground coarsely into powders. The performance of the commercial P25 TiO_2 photocatalyst (Evonik Industries, Essen, Germany) under identical testing conditions was also tested and used as the reference for

comparison. For each experiment, 10 mg of the catalyst was mixed with 80 mL of RIF solution that had a concentration of 25 mg/L. The mixture was stirred continuously in the dark to obtain a homogeneous suspension and the adsorption–desorption equilibrium. The latter was achieved after 90 min. Thereafter, the suspension was exposed to the visible light generated by the LED lamp. The UV-VIS absorption spectra of RIF solution were measured after every 30 min of exposure, which were acquired using a Jenway's 6800 double beam spectrophotometer (Cole-Parmer, Staffordshire, UK). The absorption peak at the wavelength of 472 nm in the UV-VIS spectra of RIF was used to evaluate the decrease in RIF concentration due to the photocatalytic degradation.
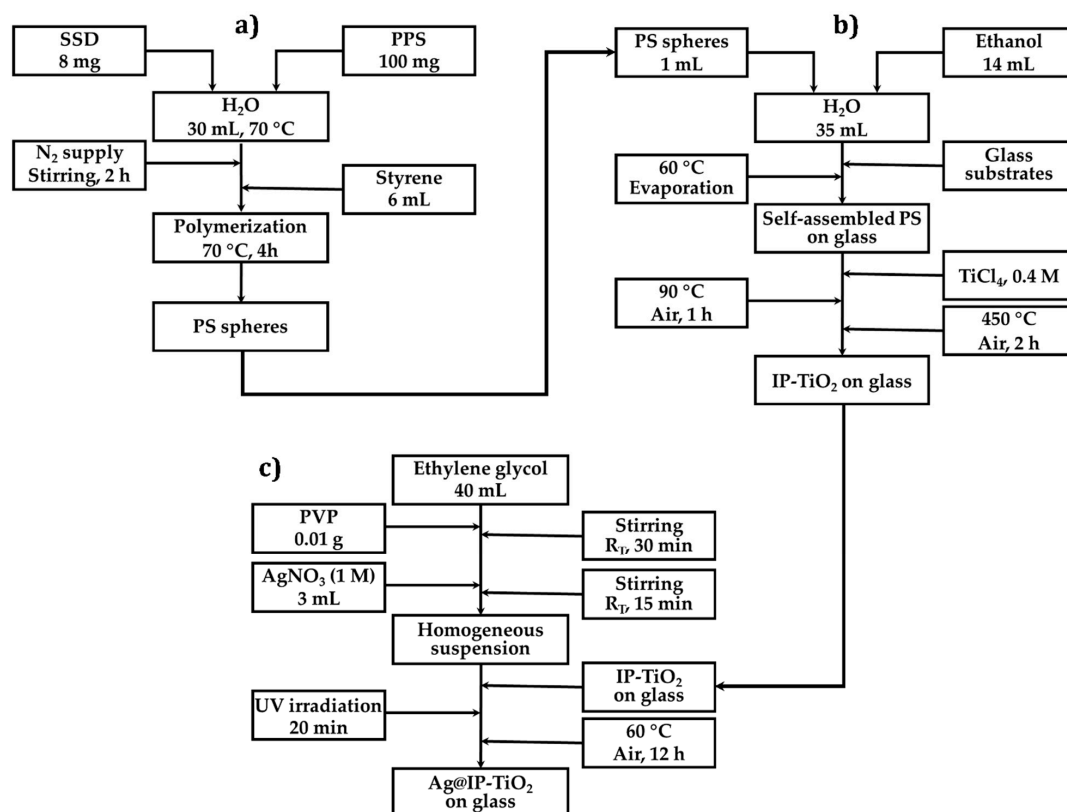
Figure 6. Schematic representation of the synthesis of (**a**) PS spheres, (**b**) IP-TiO$_2$, and (**c**) Ag@IP-TiO$_2$.
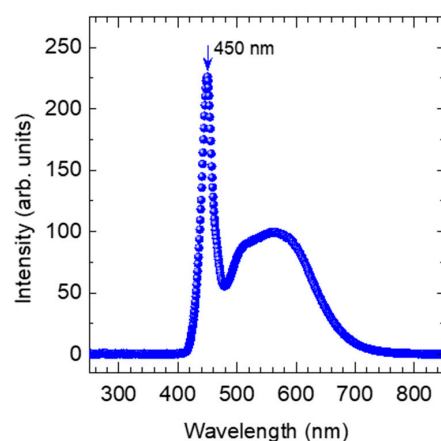
Figure 7. Emission spectrum of the LED lamp used as the light source for the photocatalytic test. The spectrum was recorded using an Ocean Optics QE65Pro Spectrometer (Ocean Insight, Orlando, FL, USA).

4. Conclusions

In summary, we have demonstrated the successful synthesis of IP-TiO$_2$ and Ag@IP-TiO$_2$ nanostructures, and the study on their crystalline structure, optical properties, and photocatalytic performance in the degradation of rifampicin antibiotic under visible-light irradiation. The results show that IP-TiO$_2$ has an anatase crystalline structure. Its UV-VIS absorption spectrum is composed of three distinguished regions, which include a band-to-band absorption with a steep edge of about 380 nm, a broad-band absorption in the wavelength range of 400–500 nm, and an extended absorption from 500 nm toward the longer wavelengths. The visible-light absorption of IP-TiO$_2$ is attributed to the presence of surface defects in coupling with the periodic inverse opal structure. This absorption facilitates the visible-light photocatalytic activity of IP-TiO$_2$, which is considerably higher than that of the commercial P25 TiO$_2$ photocatalyst. The surface modification by Ag NPs results in a significant enhancement of the photocatalytic performance of IP-TiO$_2$. This is due to the enhanced visible-light absorption and the reduced charge recombination caused by the Ag NPs, which are demonstrated by the studies on the UV-VIS absorption and PL properties of IP-TiO$_2$ and Ag@IP-TiO$_2$. The results obtained in our work not only provide further understanding of the origins of the visible-light photocatalytic activity of IP-TiO$_2$ and the enhanced performance of Ag@IP-TiO$_2$, but also demonstrate their potential application in tackling the environmental issues caused by antibiotics using visible-light photocatalysis.

Author Contributions: Conceptualization, L.L.T.N.; methodology, L.L.T.N., T.-H.T.L. and T.-T.B.; validation, L.L.T.N. and H.V.B.; formal analysis, L.L.T.N., H.V.B. and V.-D.D.; investigation, L.L.T.N., T.-H.T.L., T.-T.B. and H.V.B.; resources, L.L.T.N.; data curation, L.L.T.N. and H.V.B.; writing—original draft preparation, L.L.T.N. and H.V.B.; writing—review and editing, L.L.T.N., H.V.B. and V.-D.D.; visualization, L.L.T.N. and H.V.B.; supervision, L.L.T.N.; project administration, L.L.T.N. and H.V.B.; funding acquisition, L.L.T.N. and H.V.B. All authors have read and agreed to the published version of the manuscript.

Data Availability Statement: The data presented in this study are available on request from the corresponding author. The data are not publicly available due to privacy.

Conflicts of Interest: The authors declare no conflict of interest.

References

1. Gothwal, R.; Shashidhar, T. Antibiotic Pollution in the Environment: A Review. *Clean Soil Air Water* **2015**, *43*, 479–489. [CrossRef]
2. Kraemer, S.A.; Ramachandran, A.; Perron, G.G. Antibiotic pollution in the environment: From microbial ecology to public policy. *Microorganisms* **2019**, *7*, 180. [CrossRef] [PubMed]
3. Li, B.; Zhang, T. Biodegradation and adsorption of antibiotics in the activated sludge process. *Environ. Sci. Technol.* **2010**, *44*, 3468–3473. [CrossRef] [PubMed]
4. Wang, W.; Yu, J.; Xiang, Q.; Cheng, B. Enhanced photocatalytic activity of hierarchical macro/mesoporous TiO$_2$–graphene composites for photodegradation of acetone in air. *Appl. Catal. B Environ.* **2012**, *119–120*, 109–116. [CrossRef]
5. Schneider, J.; Matsuoka, M.; Takeuchi, M.; Zhang, J.; Horiuchi, Y.; Anpo, M.; Bahnemann, D.W. Understanding TiO$_2$ Photocatalysis: Mechanisms and Materials. *Chem. Rev.* **2014**, *114*, 9919–9986. [CrossRef]
6. Bhanvase, B.A.; Shende, T.P.; Sonawane, S.H. A review on graphene–TiO$_2$ and doped graphene–TiO$_2$ nanocomposite photocatalyst for water and wastewater treatment. *Environ. Technol. Rev.* **2017**, *6*, 1–14. [CrossRef]
7. Yang, Y.; Xu, L.; Wang, H.; Wang, W.; Zhang, L. TiO$_2$/graphene porous composite and its photocatalytic degradation of methylene blue. *JMADE* **2016**, *108*, 632–639. [CrossRef]
8. Senthil, R.A.; Theerthagiri, J.; Selvi, A.; Madhavan, J. Synthesis and characterization of low-cost g-C$_3$N$_4$/TiO$_2$ composite with enhanced photocatalytic performance under visible-light irradiation. *Opt. Mater.* **2017**, *64*, 533–539. [CrossRef]
9. Devi, L.G.; Kavitha, R. A review on non metal ion doped titania for the photocatalytic degradation of organic pollutants under UV/solar light: Role of photogenerated charge carrier dynamics in enhancing the activity. *Appl. Catal. B Environ.* **2013**, *140–141*, 559–587. [CrossRef]
10. Park, H.; Park, Y.; Kim, W.; Choi, W. Surface modification of TiO$_2$ photocatalyst for environmental applications. *J. Photochem. Photobiol. C Photochem. Rev.* **2013**, *15*, 1–20. [CrossRef]

11. Asahi, R.; Morikawa, T.; Ohwaki, T.; Aoki, K.; Taga, Y. Visible-light photocatalysis in nitrogen-doped titanium oxides. *Science* **2001**, *293*, 269–271. [CrossRef] [PubMed]

12. Asahi, R.; Morikawa, T.; Irie, H.; Ohwaki, T. Nitrogen-Doped Titanium Dioxide as Visible-Light-Sensitive Photocatalyst: Designs, Developments, and Prospects. *Chem. Rev.* **2014**, *114*, 9824–9852. [CrossRef] [PubMed]

13. Chen, X.; Liu, L.; Yu, P.Y.; Mao, S.S. Increasing Solar Absorption for Photocatalysis with Black Hydrogenated Titanium Dioxide Nanocrystals. *Science* **2011**, *331*, 746–751. [CrossRef] [PubMed]

14. Naldoni, A.; Allieta, M.; Santangelo, S.; Marelli, M.; Fabbri, F.; Cappelli, S.; Bianchi, C.L.; Psaro, R.; Dal Santo, V. Effect of nature and location of defects on bandgap narrowing in black TiO_2 nanoparticles. *J. Am. Chem. Soc.* **2012**, *134*, 7600–7603. [CrossRef]

15. Chen, X.; Liu, L.; Huang, F. Black titanium dioxide (TiO_2) nanomaterials. *Chem. Soc. Rev.* **2015**, *44*, 1861–1885. [CrossRef] [PubMed]

16. Rajaraman, T.S.; Parikh, S.P.; Gandhi, V.G. Black TiO_2: A review of its properties and conflicting trends. *Chem. Eng. J.* **2020**, *389*, 123918. [CrossRef]

17. Zhao, Y.; Yang, B.; Xu, J.; Fu, Z.; Wu, M.; Li, F. Facile synthesis of Ag nanoparticles supported on TiO_2 inverse opal with enhanced visible-light photocatalytic activity. *Thin Solid Film.* **2012**, *520*, 3515–3522. [CrossRef]

18. Wu, M.; Jin, J.; Liu, J.; Deng, Z.; Li, Y.; Deparis, O.; Su, B.L. High photocatalytic activity enhancement of titania inverse opal films by slow photon effect induced strong light absorption. *J. Mater. Chem. A* **2013**, *1*, 15491–15500. [CrossRef]

19. Lee, S.S.; Bai, H.; Liu, Z.; Sun, D.D. Optimization and an insightful properties-Activity study of electrospun TiO_2/CuO composite nanofibers for efficient photocatalytic H_2 generation. *Appl. Catal. B Environ.* **2013**, *140–141*, 68–81. [CrossRef]

20. Sordello, F.; Minero, C. Photocatalytic hydrogen production on Pt-loaded TiO_2 inverse opals. *Appl. Catal. B Environ.* **2015**, *163*, 452–458. [CrossRef]

21. Wei, Y.; Jiao, J.; Zhao, Z.; Liu, J.; Li, J.; Jiang, G.; Wang, Y.; Duan, A. Fabrication of inverse opal TiO_2-supported Au@CdS core-shell nanoparticles for efficient photocatalytic CO_2 conversion. *Appl. Catal. B Environ.* **2015**, *179*, 422–432. [CrossRef]

22. Yu, J.; Lei, J.; Wang, L.; Zhang, J.; Liu, Y. TiO_2 inverse opal photonic crystals: Synthesis, modification, and applications—A review. *J. Alloys Compd.* **2018**, *769*, 740–757. [CrossRef]

23. Wan, Y.; Wang, J.; Wang, X.; Xu, H.; Yuan, S.; Zhang, Q.; Zhang, M. Preparation of inverse opal titanium dioxide for photocatalytic performance research. *Opt. Mater.* **2019**, *96*, 109287. [CrossRef]

24. Fiorenza, R.; Bellardita, M.; Scirè, S.; Palmisano, L. Photocatalytic H_2 production over inverse opal TiO_2 catalysts. *Catal. Today* **2019**, 113–119. [CrossRef]

25. Temerov, F.; Ankudze, B.; Saarinen, J.J. TiO_2 inverse opal structures with facile decoration of precious metal nanoparticles for enhanced photocatalytic activity. *Mater. Chem. Phys.* **2020**, *242*. [CrossRef]

26. Zul, A.; Temerov, F.; Saarinen, J.J. Multilayer TiO_2 Inverse Opal with Gold Nanoparticles for Enhanced Photocatalytic Activity. *ACS Omega* **2020**, *5*, 11595–11604. [CrossRef]

27. Li, Y.; Piret, F.; Léonard, T.; Su, B.-L. Rutile TiO_2 inverse opal with photonic bandgap in the UV–visible range. *J. Colloid Interface Sci.* **2010**, *348*, 43–48. [CrossRef] [PubMed]

28. Temerov, F.; Pham, K.; Juuti, P.; Mäkelä, J.M.; Grachova, E.V.; Kumar, S.; Eslava, S.; Saarinen, J.J. Silver-Decorated TiO_2 Inverse Opal Structure for Visible Light-Induced Photocatalytic Degradation of Organic Pollutants and Hydrogen Evolution. *ACS Appl. Mater. Interfaces* **2020**, *12*, 41200–41210. [CrossRef]

29. Ye, J.; He, J.; Wang, S.; Zhou, X.; Zhang, Y.; Liu, G.; Yang, Y. Nickel-loaded black TiO_2 with inverse opal structure for photocatalytic reduction of CO_2 under visible light. *Sep. Purif. Technol.* **2019**, *220*, 8–15. [CrossRef]

30. Cheng, P.; Yang, Z.; Wang, H.; Cheng, W.; Chen, M.; Shangguan, W.; Ding, G. TiO_2-graphene nanocomposites for photocatalytic hydrogen production from splitting water. *Int. J. Hydrogen Energy* **2012**, *37*, 2224–2230. [CrossRef]

31. Chen, Z.; Fang, L.; Dong, W.; Zheng, F.; Shen, M.; Wang, J. Inverse opal structured Ag/TiO_2 plasmonic photocatalyst prepared by pulsed current deposition and its enhanced visible light photocatalytic activity. *J. Mater. Chem. A* **2014**, *2*, 824–832. [CrossRef]

32. Orilall, M.C.; Abrams, N.M.; Lee, J.; DiSalvo, F.J.; Wiesner, U. Highly crystalline inverse opal transition metal oxides via a combined assembly of soft and hard chemistries. *J. Am. Chem. Soc.* **2008**, *130*, 8882–8883. [CrossRef]

33. Kang, J.; Kim, J.; Lee, S.; Wi, S.; Kim, C.; Hyun, S.; Nam, S.; Park, Y.; Park, B. Breathable Carbon-Free Electrode: Black TiO_2 with Hierarchically Ordered Porous Structure for Stable Li–O_2 Battery. *Adv. Energy Mater.* **2017**, *7*, 1700814. [CrossRef]

34. Reddy, K.M.; Manorama, S.V.; Reddy, A.R. Bandgap studies on anatase titanium dioxide nanoparticles. *Mater. Chem. Phys.* **2003**, *78*, 239–245. [CrossRef]

35. Curti, M.; Mendive, C.B.; Grela, M.A.; Bahnemann, D.W. Stopband tuning of TiO_2 inverse opals for slow photon absorption. *Mater. Res. Bull.* **2017**, *91*, 155–165. [CrossRef]

36. Liqiang, J.; Yichun, Q.; Baiqi, W.; Shudan, L.; Baojiang, J.; Libin, Y.; Wei, F.; Honggang, F.; Jiazhong, S. Review of photoluminescence performance of nano-sized semiconductor materials and its relationships with photocatalytic activity. *Sol. Energy Mater. Sol. Cells* **2006**, *90*, 1773–1787. [CrossRef]

37. Zhao, Y.; Li, C.; Liu, X.; Gu, F.; Jiang, H.; Shao, W.; Zhang, L.; He, Y. Synthesis and optical properties of TiO_2 nanoparticles. *Mater. Lett.* **2007**, *61*, 79–83. [CrossRef]

38. Xu, J.; Li, L.; Yan, Y.; Wang, H.; Wang, X.; Fu, X.; Li, G. Synthesis and photoluminescence of well-dispersible anatase TiO_2 nanoparticles. *J. Colloid Interface Sci.* **2008**, *318*, 29–34. [CrossRef]

39. Guo, J.; Benz, D.; Doan Nguyen, T.T.; Nguyen, P.H.; Thi Le, T.L.; Nguyen, H.H.; La Zara, D.; Liang, B.; Hintzen, H.T.; van Ommen, J.R.; et al. Tuning the photocatalytic activity of TiO$_2$ nanoparticles by ultrathin SiO$_2$ films grown by low-temperature atmospheric pressure atomic layer deposition. *Appl. Surf. Sci.* **2020**, *530*, 147244. [CrossRef]

40. Pallotti, D.K.; Passoni, L.; Maddalena, P.; Di Fonzo, F.; Lettieri, S. Photoluminescence Mechanisms in Anatase and Rutile TiO$_2$. *J. Phys. Chem. C* **2017**, *121*, 9011–9021. [CrossRef]

41. Zhang, J.; Zhou, P.; Liu, J.; Yu, J. New understanding of the difference of photocatalytic activity among anatase, rutile and brookite TiO$_2$. *Phys. Chem. Chem. Phys.* **2014**, *16*, 20382–20386. [CrossRef]

42. Hirakawa, T.; Kamat, P.V. Charge separation and catalytic activity of Ag@TiO$_2$ core-shell composite clusters under UV-irradiation. *J. Am. Chem. Soc.* **2005**, *127*, 3928–3934. [CrossRef]

43. Guo, J.; Yuan, S.; Yu, Y.; Van Ommen, J.R.; Van Bui, H.; Liang, B. Room-temperature pulsed CVD-grown SiO$_2$ protective layer on TiO$_2$ particles for photocatalytic activity suppression. *RSC Adv.* **2017**, *7*, 4547–4554. [CrossRef]

44. Stets, S.; do Amaral, B.; Schneider, J.T.; de Barros, I.R.; de Liz, M.V.; Ribeiro, R.R.; Nagata, N.; Peralta-Zamora, P. Antituberculosis drugs degradation by UV-based advanced oxidation processes. *J. Photochem. Photobiol. A Chem.* **2018**, *353*, 26–33. [CrossRef]

45. Singh, J.; Tripathi, N.; Mohapatra, S. Synthesis of Ag–TiO$_2$ hybrid nanoparticles with enhanced photocatalytic activity by a facile wet chemical method. *Nano Struct. Nano Objects* **2019**, *18*, 100266. [CrossRef]

46. Chen, Y.; Feng, L. Silver nanoparticles doped TiO$_2$ catalyzed Suzuki-coupling of bromoaryl with phenylboronic acid under visible light. *J. Photochem. Photobiol. B Biol.* **2020**, *205*, 111807. [CrossRef]

47. Awazu, K.; Fujimaki, M.; Rockstuhl, C.; Tominaga, J.; Murakami, H.; Ohki, Y.; Yoshida, N.; Watanabe, T. A plasmonic photocatalyst consisting of silver nanoparticles embedded in titanium dioxide. *J. Am. Chem. Soc.* **2008**, *130*, 1676–1680. [CrossRef]

48. Cho, S.A.; Jang, Y.J.; Lim, H.D.; Lee, J.E.; Jang, Y.H.; Nguyen, T.T.H.; Mota, F.M.; Fenning, D.P.; Kang, K.; Shao-Horn, Y.; et al. Hierarchical Porous Carbonized Co$_3$O$_4$ Inverse Opals via Combined Block Copolymer and Colloid Templating as Bifunctional Electrocatalysts in Li–O$_2$ Battery. *Adv. Energy Mater.* **2017**, *7*, 1700391. [CrossRef]

49. Nédez, C.; Ray, J.L. Efficient removal of polymerization inhibitors by adsorption on the surface of an optimized alumina. *Langmuir* **1999**, *15*, 5932–5936. [CrossRef]

50. Sofianou, M.V.; Boukos, N.; Vaimakis, T.; Trapalis, C. Decoration of TiO$_2$ anatase nanoplates with silver nanoparticles on the {101} crystal facets and their photocatalytic behaviour. *Appl. Catal. B Environ.* **2014**, *158–159*, 91–95. [CrossRef]